Failure mechanisms in cobalt welded with a silver–copper filler

ARTICLE · OCTOBER 2015

DOI: 10.1016/j.msea.2015.07.094

3 AUTHORS:

Everett M. Criss

University of California, San Diego

6 PUBLICATIONS **6** CITATIONS

SEE PROFILE

Richard Smith

University of Nottingham

30 PUBLICATIONS **59** CITATIONS

SEE PROFILE

Marc A Meyers

University of California, San Diego

484 PUBLICATIONS **11,198** CITATIONS

SEE PROFILE

Materials Science & Engineering A 645 (2015) 369–382

Contents lists available at ScienceDirect

Materials Science & Engineering A

journal homepage: www.elsevier.com/locate/msea

Failure mechanisms in cobalt welded with a silver–copper filler

Everett M. Criss [a,*], Richard J. Smith [d], Marc A. Meyers [a,b,c]

[a] Department of Mechanical and Aerospace Engineering, University of California, San Diego, La Jolla, USA
[b] Materials Science and Engineering Program, University of California, San Diego, La Jolla, USA
[c] Department of Nanoengineering, University of California, San Diego, La Jolla, USA
[d] Electrical Systems and Optics Research Division, Faculty of Engineering, University of Nottingham, Nottingham, Nottinghamshire, United Kingdom

ARTICLE INFO

Article history:
Received 16 April 2015
Received in revised form
28 July 2015
Accepted 30 July 2015
Available online 31 July 2015

Keywords:
Cobalt
Silver–copper
Welding surrogacy
Tungsten inert gas welding
Residual stress
Weld fracture

ABSTRACT

Cobalt silver–copper (Co–AgCu) weldments approximate the stresses and failure mechanisms of beryllium aluminum–silicon (Be–AlSi) welds, which have strategic importance but are hazardous to study. Failure tests of these surrogate Co–AgCu welds, examined in tension and four-point bending, show that residual stresses and post-welding heat treatment have little or no effect on strength, whereas weld quality and geometry are extremely important. Scanning electron microscopy images reveal abundant defects in poor welds, which usually fail through propagation of preexisting cracks. Fracture surfaces show a variety of morphologies, ranging from dimples in the AgCu filler, to cleavage steps in the CoCu peritectic, and suspected intergranular fracture in the cobalt base. Spatially resolved acoustic spectroscopy reveals significant changes in microstructure near the base–filler interface, whereas wavelength dispersive analysis shows high Cu concentrations in this area.. Contrary to finite element predictions, these welds were found to be stronger during face bending than root bending, likely resulting from the increased number of cracks and imperfections in the Co base. These computations correctly predict that weld strength depends on geometry and that welds fail either in the cobalt base, or along the base–filler interface. Crack compliance measurements show that the largest residual stresses are located along this interface. However, these stresses are unlikely to influence failure due to their direction, whereas stresses in the weld root are too small to have observable effects on failure. The strength of Co–AgCu welds depends strongly on geometry, penetration, and weld quality, but little on residual stresses, and this conclusion is tentatively extended to Be–AlSi welds.

1. Introduction and Goals

The cobalt silver–copper (Co–AgCu) welding system was developed as a surrogate for beryllium aluminum–silicon (Be–AlSi) welds in order to improve understanding of the toxic Be–AlSi system without use of special facilities and risk of illness [1,2]. In this surrogate concept, Co–AgCu must mimic, as accurately as possible, the behavior of Be–AlSi, including the interactions between the Be base and the AlSi filler. Cobalt is an ideal surrogate for beryllium-based weldments, due to the mechanical, thermal and crystallographic similarities of the two elements. Both cobalt and beryllium have a hexagonally close packed crystal structure (HCP), which endows both elements with relatively high stiffness and similar melting points [3–5]. Behavior of the Ag–Cu filler during welding is also of interest because silver–copper filler metal in cobalt welds was found to best emulate the chemistry of the Be–AlSi system, as both systems are characterized by a lack of miscibility between filler and base metals [1]. Furthermore, the mismatches in the coefficient of thermal expansion (CTE) and Young's modulus (E) between AgCu and Co are similar, although not as extreme, as the mismatches of CTE and E in the Be–AlSi system. Criss and Meyers [1] provide a detailed description of surrogate development, welding techniques, and why the Co–AgCu surrogate can simulate the behavior of Be–AlSi rings, PIGMA welded at Los Alamos National Laboratory.

The study of Co and specifically its behavior during welding is important for other reasons. Cobalt is used as an alloying element in a variety of steels, carbides, and corrosion resistant alloys [4], and is a primary constituent of batteries, magnets, and superalloys [6–8]. Cobalt–chromium–molybdenum alloys (e.g. Vitallium, Megallium) are used in dentistry and biomedical implants [9]. Vitallium is usually joined via soldering or brazing [9], but may be joined by torch [10] or TIG [11]. Cobalt–chromium base alloys (Stellite) are generally used as hardfacings, which are applied using a variety of welding, cladding and brazing techniques [12,

* Corresponding author.
E-mail address: ecriss@ucsd.edu (E.M. Criss).

http://dx.doi.org/10.1016/j.msea.2015.07.094
0921-5093/

13]. Heat resistant alloys, often consisting of Co–Cr–Ni–W, are also welded or brazed [4].

The eutectic, AgCu filler metal is commonly used as a filler for vacuum brazing [14]. Silver–copper alloys are also used in jewelry and tableware [e.g., sterling silver (92.5% Ag); 15], and as electrical contact alloys [16].

Despite the diverse usage of the components of our Co–AgCu system, information is lacking on the brazing of cobalt–copper, due to possible liquid metal embrittlement [17], and welding regarding HCP cobalt base alloys. A majority of cobalt's structural alloys (e.g. Stellite, Vitallium) utilize the high temperature face centered cubic (fcc) phase [17], and differ structurally from pure cobalt, which is HCP. Cobalt usage in batteries usually involves cobalt oxide, cobalt hydroxide or lithiated cobalt oxide (Li_xCoO_2) [4,18], all of which differ from pure cobalt structurally and chemically. Some samarium-cobalt magnets ($SmCo_5$) do possess a hexagonal crystal structure [19], but are not welded. As such, there is limited information regarding fabrication and welding of pure cobalt. Because development of Co based superalloys is ongoing [20,21], understanding the behavior of the pure metal is important.

In this paper, the Co–AgCu system is used to investigate the effects that residual stress, weld geometry, weld quality, and post welding heat treatment have on weld failure, and it extrapolates these results to welded Be–AlSi. Geometric effects are expected to be of importance, since their influence on weld failure is known (e.g., [22–24]). The welding techniques discussed in the previous work [1], were used to create 11 new welds, which were analyzed alongside the single complete weld from the previous study.

The present work utilizes tension and 4-point bending to produce weld failures in the Co–AgCu weldments, and combines these tests with the crack compliance (slitting) method to determine the effect of residual stresses. The weldments are further characterized using scanning electron microscopy (SEM) and wavelength dispersive analysis (WDS), by developing a novel use of optical microscopy, and by applying a recently developed method, spatially resolved acoustic spectroscopy (SRAS). SRAS is a laser ultrasonic technique which produces maps of the surface acoustic wave velocity (SAW) [25,26]. The SAW velocity for a particular propagation direction depends strongly on the crystallographic orientation of the material and so can be used to map the microstructure of a material. Combining a number of velocity maps with different acoustic wave propagation directions can generate information about the *c*-axis orientation for hexagonal materials, or the complete grain orientation for some specific crystallographic symmetries [26].

Effects of low temperature heat treatment on weld strength are examined, in order to determine whether residual stress amelioration is possible. Finite element models were constructed to understand our residual stress measurements and fracture results. This combination of measurements, images and quantitative models shows that residual stresses do not substantially impact failure in Co–AgCu weldments, but that weld geometry, material quality, and defects and imperfections govern weld strength and failure. The insight provided by this report into the behavior of welded cobalt pertains to development and joining of new cobalt alloys, as well as the behavior of the original Be–AlSi system.

2. Experiments and techniques

2.1. Materials

The weld base was 99.95% pure cobalt, hot rolled to 7.6 mm (Sophisticated Alloys). The cobalt plate was then heat treated at 325 °C for 100 h to homogenize the grain structure of our metal.

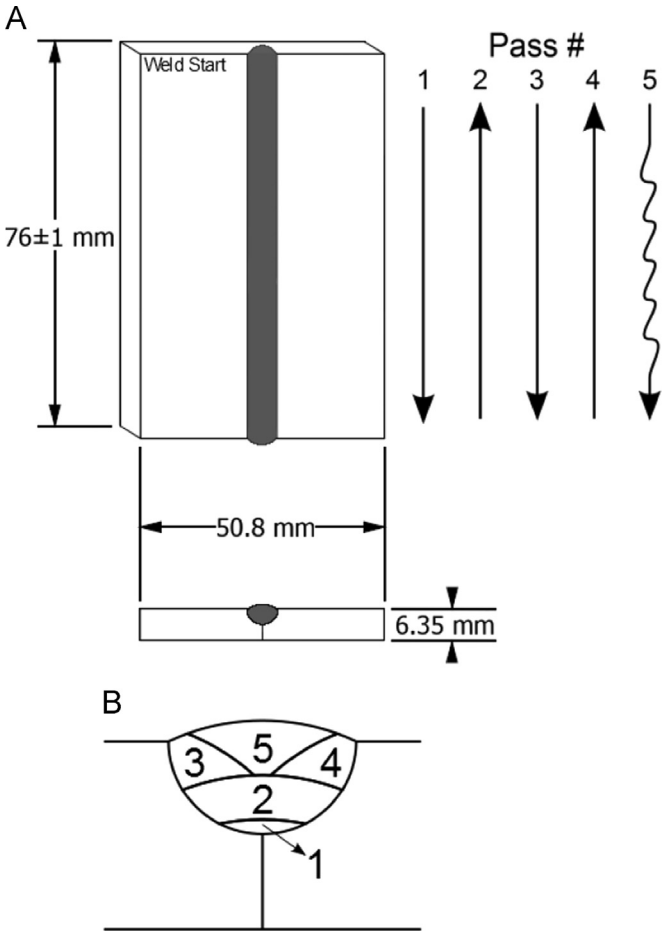

Fig. 1. A: Pass locations, directions, and weldment geometry used in the Co–AgCu TIG welds. Two cobalt samples sharing a single U-groove are joined by 5 passes in alternating directions. The final, oscillating pass is indicated by a wavy line. B: Approximate weld-bead locations. Dimensions are all ±0.08 mm unless noted otherwise.

Some studies [27] have reported the persistence of the FCC phase after refining the grain structure by rolling, but our previous x-ray measurements indicate that minimal FCC is present after this heat treatment [1].

The filler wire was 72–28% AgCu (obtained from Lucas Milhaupt), which is at the eutectic point. It is available from a number of sources, and is often referred to by its AWS specification, BAg-8 [28].

2.2. Welding equipment, materials and parameters

Eleven additional welds were produced. Our welding setup, materials and geometry are identical to the previous study [1], where they are described in more detail. All welds were produced by a single ASME aerospace certified welder. He employed a TIG welder with high frequency stabilization (Miller Aerowave), which was set to direct current electron negative (DCEN).

All welds utilized two standard parts, each consisting of a 76 mm long, 25.4 mm wide, 6.25 mm thick block of 99.95% cobalt with a 3.2 mm radius J-groove (Fig. 1). The thicknesses of the J-groove and part were verified accurate to 0.08 mm.

Prior to welding, the parts were positioned above a heated, porous refractory substrate with a purpose built clamp. The clamp was furnace heated to above 300 °C, the parts were loaded at approximately 250 °C, and welding occurred at a substrate temperature of approximately 230 °C.

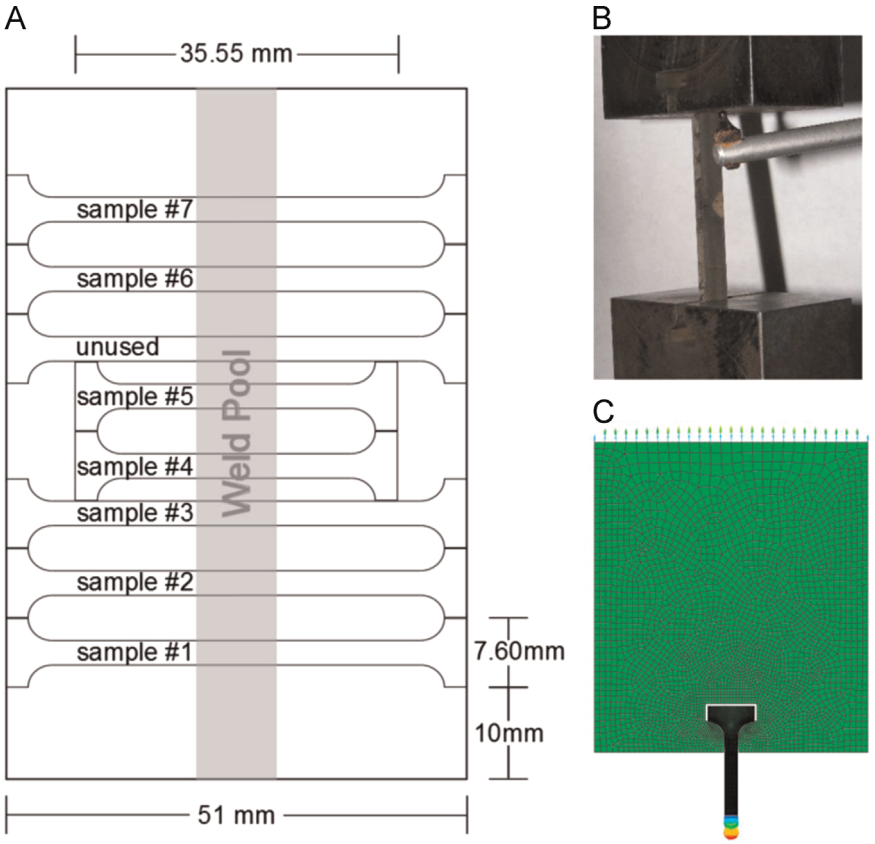

Fig. 2. Tension test pieces, tension test, and FEA model. A: Locations and size of test pieces. B: Test piece being fractured in tension grips, showing location of filler pool, and use of deflectometer. C: FEA model showing half symmetry test piece in tension. The large green area is our fixture, the test piece is dark due to the small size of its mesh. Colored area at the bottom are force vectors due to symmetric boundary conditions. (For interpretation of the references to color in this figure legend, the reader is referred to the web version of this article.)

All welds involve 5 passes, in alternating directions, with 0.25 l/s Ar back-gas and He or Ar top-gas (Fig. 1). Passes 1–4 were done at 225 A, with 0.43 l/s He top-gas, while pass 5 was 150 A with 0.25 l/s Ar top-gas. Passes 1 and 2 were centered, whereas passes 3 and 4 were to either side of the original J-groove (Fig. 1B). The final pass was done in an oscillating trajectory. The weldments were allowed to cool to room temperature after passes 2, 3, and 4.

2.3. Fracture in tension and 4-point bending

Welds were fractured both in tension and in a 4-point bending apparatus, using an Instron 3307 tensile tester. To perform the tension test, the weld was first precision ground until it had an orthogonal cross section. It was then sectioned in an electrical discharge machine (EDM) into 8 test pieces (Fig. 2A), and loaded into a specially made fixture (Fig. 2B).Displacement was measured with a deflectometer (Fig. 2B). Results were compared to finite element models (Fig. 2C).

Four-point bending was performed on 8 different welds, using both transverse root bending (Fig. 3A) and transverse face bending (Fig. 3B), on heat treated and as is weldments. These orientations correspond to the ASTM weld bending standard [29], although the testing jig here differs by having 4 rollers (Fig. 3) rather than a guided bend fixture. For brevity, these tests will be referred to as root bending and face bending, respectively. The root bending test is identical to the fracture tests performed previously [1], although the samples are new. The tester was set to a 48 mm support span, and a 12 mm load span. No extensometer was fitted, which will result in accurate load data, but overestimated displacement data.

One weld was EDM cut into 20 sections but not ground

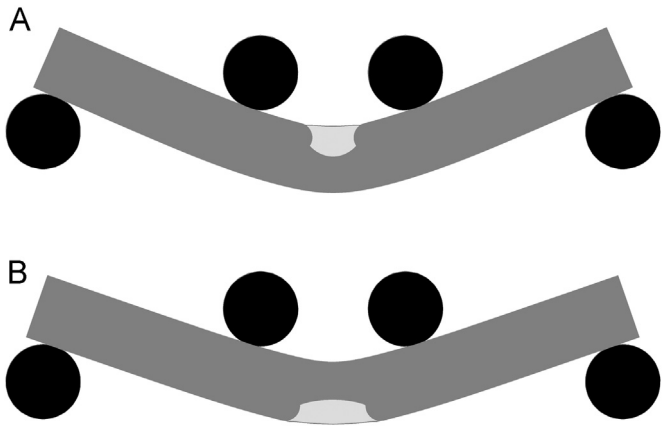

Fig. 3. Traverse Root (A) and Face bending (B) orientations. AISI 304 steel rollers (dark), sample (medium) and filler (light).

(Fig. 4A). Fracture was performed in the root bending orientation, and compared to a sample from our previous work [1].

Three welds were ground until flat, and then cut with an EDM into 21 sections (Fig. 4B). We alternately applied root and face bending to adjacent sections. Results were compared to finite element models.

Four welds were used in a combined residual stress and heat treatment study. These welds were also ground, before being sectioned into 4 fracture and 4 residual stress specimens (Fig. 4B). Half of the fracture specimens and half of the residual stress specimens were heat treated at 325 ± 2 °C for 100 h. Fracture was

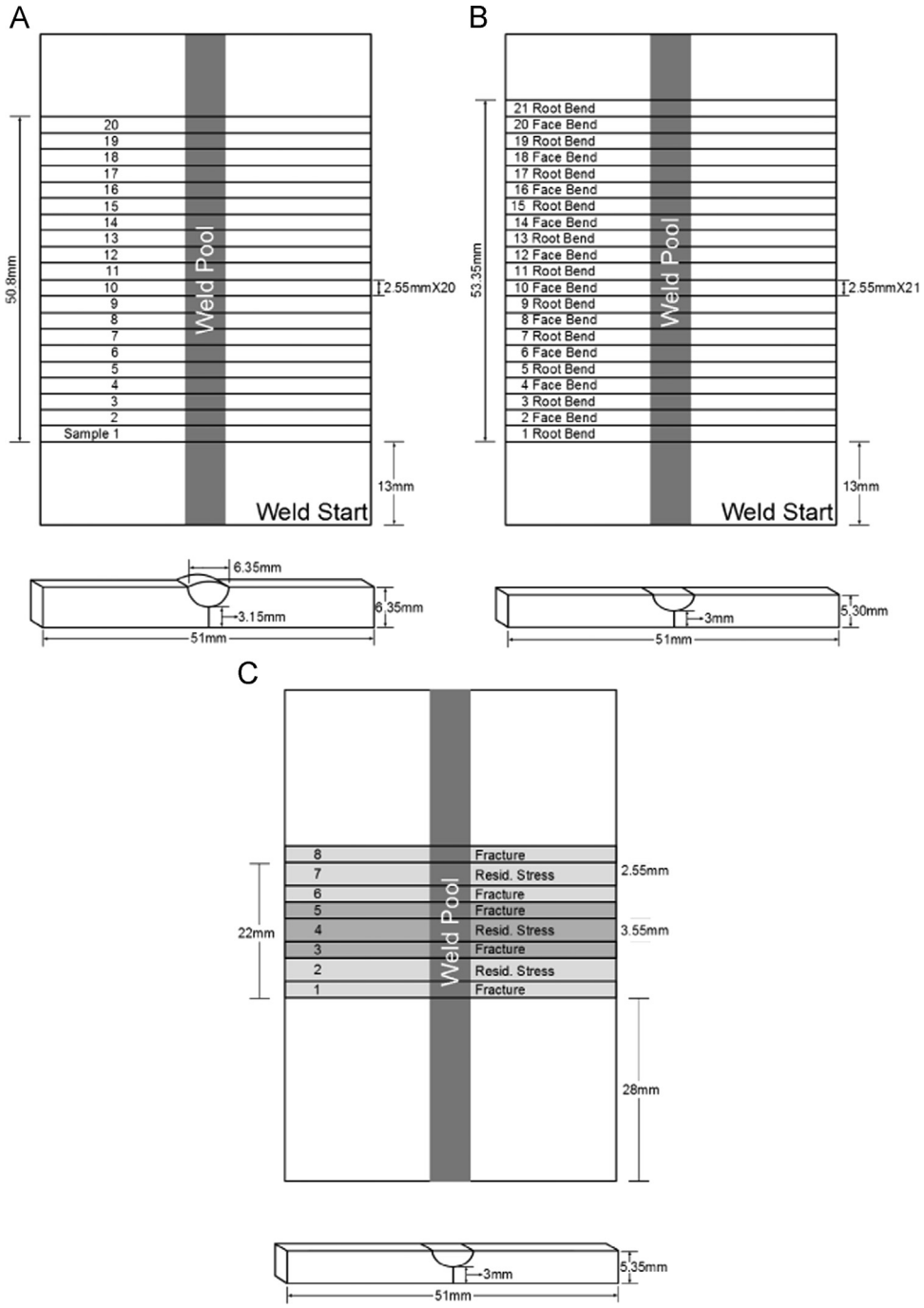

Fig. 4. A: Schematic shows section positions and dimensions for the 20 section, unground root bending test. B: Schematic shows section positions and dimensions for the 21 section alternating face and root bending test. C: Schematic shows section positions, dimensions and heat treatments for the crack compliance method and root bending tests. Either sections 3–5, or 1–2, 6–8, were heat treated as indicated by the different shading.

performed in the root bending orientation. Results were compared to finite element models.

2.4. Scanning electron microscopy (SEM) and energy dispersive X-ray spectroscopy (EDS)

Imaging and compositional analysis was performed on a Phillips XL30 ESEM with an Oxford EDS attachment. Images were taken after fracture in tension and 4-point bending utilizing secondary electrons. For face and root bending, only the strongest and weakest sections were examined. Prior to microscopy, these sections were polished and coated with iridium. Fractography was also performed after tension, on the uncoated failure surface of the strongest test piece. Compositional analysis was performed at areas of interest utilizing the EDS attachment. Concentrations of Ag, C, Co, Cu and O were measured, but percentages of C and O were removed during analysis.

2.5. Optical microscopy

To reveal machining inconsistency, as well as sufficiently large grain structures, we developed a new method of sample preparation involving first grinding the weld to a high degree of flatness using a granite block and 1500 grit paper. Once this is

complete, a slurry is prepared from a mixture of silicon carbide, alumina, and water. Carefully removing the sample from the polishing surface allowed surface tension to adhere the slurry to the sample, which revealed surface deviations during optical microscopy. Although this method does not reveal fine detail, it is faster than etching, and can be performed utilizing only sandpaper, polishing compound, a polishing block, and a camera with a macro lens.

2.6. Spatially resolved acoustic spectroscopy (SRAS)

Two welds were sectioned along the direction of welding, in the weld center. Two SRAS scans were performed on each weld, one with the wave propagation direction aligned with the long edge of the sample and the other orthogonal to this. The projected fringe pattern had a spacing of 23.6 μm and so the measured acoustic frequency range was ~100 to 140 MHz. The acoustic generation patch size was 120 μm giving a spatial resolution on the order of 60 μm.

The weldments studied have a predominantly hexagonally close packed cobalt base. Due to the geometry of this crystal structure, SRAS can provide some indication of *c*-axis orientation by combining two maps with orthogonal propagation directions. Regions where the measured surface acoustic wave velocity is 'fast' for both propagation directions are basal, for 'fast/slow' or 'slow/fast' combinations the *c*-axis lies orthogonal or in line with the scan direction respectively.

During the SRAS scan the amount of reflected probe light is also recorded, this allows a high contrast/high resolution optical image to be obtained; these are high contrast images showing surface features such as the base–filler boundary and crack locations.

2.7. Electron microprobe and wavelength dispersive analysis (WDS)

A weld section from the previous study [1] was characterized by wavelength dispersive analysis (WDS) and standard procedures on the JXA-8200 electron microprobe at Washington University, using "Probe for EPMA" for data reduction (see http//www.probesoftware.com/). The measured data were corrected with CITZAF after [30]. Pure Ag and Co were used as standards for their respective elements, while cartridge brass (NIST) was used as our Cu standard.

Locations of the WDS measurements are overlaid on micrographs of the weld section, created using electron backscatter as well as optical microscopy. Optical micrographs were taken after the weldment was sequentially etched by an aqua regia based mixture and nital. Full description of the methods used to produce these images is given in [1]. Electron backscatter images were created using the microprobe software described above.

2.8. Finite element analysis (FEA) of fracture

Three sets of finite element fracture models were created using Abaqus. The first set of models consists of three dimensional representations of the tension test. The second set are two-dimensional representations of the face and root bending tests. The third set are also 2d representations of the root bending tests used in the residual stress study.

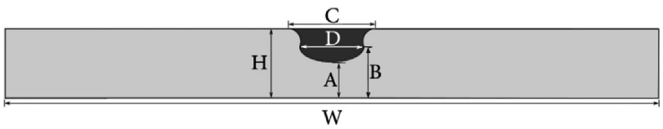

Fig. 5. Basic shape used in all of our FEA. This corresponds roughly to the observed shapes of our weld sections. Table 1 provides parameter values.

In order to develop models that are relevant to all of our results, we assumed a generic filler shape for all computations (Fig. 5) that is typical of all our welds. Shape parameters were determined by a combination of mechanical and optical measurement over the sample set being investigated. Measurements are accurate to 0.025 mm, but the variance across parts significantly exceeds that value. To estimate the uncertainties in our predictions, multiple models were produced per sample set, based on these measurements (Table 1). For bending tests, these models represent what we believe are the average, weakest, and strongest possible geometries. For the weakest FEA geometry, we utilized measurements providing maximum filler area, and minimum base area. For the strongest geometry, we utilized measurements forming the smallest filler, and largest base. The average model was constructed by simple averaging our measurements. For tension, only the average dimensions from the measured test pieces were used in our models.

All of these FEA models utilize material properties for the base, filler and fixtures (Table 2) as previously discussed [1]. The base of the weld was assumed to be pure cobalt. Cobalt elastic parameters were taken from [3], whereas plastic data was taken from [31] and modified [1]. The rollers and tensile fixture were assumed to be completely elastic, AISI 304 steel [1, 3]. The elastic properties of the filler were taken as a Voigt-Reuss-Hill average of data [3] as described in [1]. The plastic properties of the filler were taken from tensile measurements [32] and corrected [1]. Basic metal plasticity, as defined by Abaqus based on the von Mises criterion, was used for the cobalt base and AgCu filler. Contact between the sample and fixtures was assumed to be frictionless, with the cobalt and filler being defined as the slave surfaces, and the steel fixture defined as the master surface. As a result of the large deformations and nonlinear behavior observed in our specimens, it was necessary to incorporate both plasticity and contact into our models.

All models were displacement, not force controlled, and used the standard, implicit problem solver.

2.8.1. Tension FEA

The two tension models were 3-dimensional, and utilized mirror symmetry across the weld (Fig. 2). Each of these models corresponds to the different types of tension sample (Fig. 2). Geometry for the fixture was measured via calipers, as were the width, height and depth of these samples (Table 1). Filler geometry was measured optically from approximately 30 mm and 45 mm from the weld start. All elements were hexagonal, corresponding to a seed size of between 0.1 mm and 0.125 mm (Table 3). In order to stabilize the FEA, a minimum of 250 steps were used in both calculations.

2.8.2. Face and root 4 point bending FEA

The models used for 4-point bending were 2-dimensional, and constructed of 5 parts consisting of a sample and 4 rollers. The face and root 4-point bending tests are identical, with the exception that the sample was flipped. Geometry of the rollers was measured via caliper, as were the height and depth of all of the samples. Width is approximate, and does not influence model behavior. The filler parameters were measured optically, from images occurring approximately 13 mm and 66 mm from the weld start. Final values were created from the maximum, minimum and average dimensions from the three welds used in the corresponding study (Table 1). Basic finite element parameters are provided (Table 3).

2.8.3. Root 4 point bending (residual stress study) FEA

Models used for 4-point bending were 2-dimensional, and constructed of 5 parts consisting of a sample and 4 rollers. Geometry of the rollers was measured via caliper, as were the height

Table 1
FEA Geometry, ±0.005 mm.

Finite element model	Width (*W*), mm	Height (*H*), mm	Thickness into page, mm	*A*, mm	*B*, mm	*C*, mm	*D*, mm
Tension, average (long test piece)	N/A	5.36	2.075	3.04	4.335	6.47	4.63
Tension, average (short test piece)	N/A	5.36	2.055	3.04	4.335	6.47	4.63
Root and face bending, weakest	50.08	5.26	2.11	2.61	3.36	8.02	6.43
Root and face bending, average	50.08	5.31	2.125	2.985	3.71	6.91	4.73
Root and face bending, strongest	50.08	5.335	2.135	3.435	3.94	5.69	3.88
Root bending and crack compliance, weakest	50.08	5.32	2.465	2.465	3.63	8.28	5.58
Root bending and crack compliance, average	50.08	5.355	2.505	2.76	3.945	6.85	5.04
Root bending and crack compliance, strongest	50.08	5.385	2.525	3.075	4.36	5.74	3.94

Table 2
FEA material parameters (4 significant figures).

Material	Location	Young's modulus (GPa)	Poisson's ratio	Plasticity law	UTS (MPa)	Max equivalent plastic strain
AISI 316	Rollers/tensile fixture	215	0.283	N/A	N/A	N/A
Cobalt	Weld base	211	0.32	Mises	949.1	0.1727
72/28 AgCu	Weld filler	95.37	0.3593	Mises	302	0.3136

and depth of all of the samples. Width is approximate, and does not influence model behavior. The filler parameters *B* and *C* were measured optically, while parameters *A* and *D* were measured via caliper from images occurring approximately 28 mm and 52 mm from the weld start. Final values were created from the maximum, minimum and average dimensions from the four welds used in the residual stress study (Table 1). Basic finite element parameters are provided (Table 3).

2.9. Crack compliance method

Residual stress measurements were successful performed on samples from three separate welds utilizing the crack compliance, or slitting method. This method combines incremental strain measurements with analytic or finite element analysis assisted data reduction [33]. In our case, we combined incremental cuts using a wire EDM, with FEA data reduction using Abaqus.

2.9.1. Strain measurements

To perform the strain measurements, the welds were first cut into eight sections using an EDM (Fig. 4). Half of these sections were heat treated, half were not. Three of these sections were used for residual stress measurements, the others were fractured (Fig. 4). This resulted in 12 total residual stress measurements. Of these 12 tests, only 5 were successful, mainly due to water impinging on the strain gauge.

For all of these tests, a strain gauge (Micro-Measurements EA-06-062AK-120) was mounted on section, and protected via watertight acrylic coating. The sections were degreased with methyl–ethyl–ketone, before being cleaned with a mild phosphoric-acid compound (Conditioner A). This compound was then removed with an ammonia-based neutralizer (Neutralizer 5A). The glue used to affix the samples was high purity cyanoacrylate (CN general purpose adhesive). The sections were then protected by a watertight acrylic coating (M-Coat D). Gauges were mounted on the back face of the section, in the exact center, on the cobalt base. This is similar to the typical setup used at Los Alamos [34], with the omission of a top gauge.

The sections were then loaded into a flushing type EDM. After the machine was automatically zeroed, a crack was extended from the filler to the base, using 20 increments of 0.25 mm each. Utilizing any more increments would jeopardize the strain gauge by potentially cutting the section in half.

The pressure of the jets, combined with the tight tolerances between the gauge size and part width, contributed to the destruction of the first 6 gauges. The next 6 gauges were run under minimal pressure; 1 additional gauge was lost due to poor sample-gauge adhesion.

Residual stress measurements were taken after each increment. In order to account for EDM induced thermal expansion, measurements were taken after a time delay, or after observed temperature equilibration. The first 8 tests utilized a time delay; measurements were taken until no change was observed over a 2 min period. This generally occurred after 6 or 8 min. The final four tests were temperature controlled via a mounted thermocouple. Measurements were taken between 23.4 °C and 23.6 °C.

The procedure used during testing is very similar to the method in use at Los Alamos [34]. Our procedure differs in our use of temperature control, our omission of a top gauge, and our lack of post-test optical measurements.

2.9.2. Data reduction

Due to the complex shape of our part it was necessary to utilize FEA to analyze our strain data. Utilization of FEA for data reduction is typical for the crack compliance method [33]. FEA models for strain data reduction were created using the same shape parameters as earlier (Section 2.8, Table 1). Variance in calculated residual stresses due to these shape parameters is not significant, with the peak tensile stresses generally within ±5% of each other. This is a considerable under-representation of experimental uncertainties during strain measurement.

These models are 2-dimensional, and utilize weld symmetry for stress computation. Element size is restricted due to the requirement that crack width (induced by the EDM wire) be effectively filled. This results in a seed size of 0.1 mm (Table 3).

In order to reduce the strain data, the model is started in a stress free state. The crack is simulated through element removal. A sequential, unit traction is then applied to every set of faces exposed through elemental removal. The change in displacement is then recorded over the elements representing the strain gauge contact area.

This allows creation of a compliance matrix, relating relieved residual stresses and measured strains. By solving for residual stresses using this compliance matrix, our residual stress results were created.

3. Results and discussion

3.1. Spatially resolved acoustic spectroscopy, optical microscopy, and electron microprobe on unfractured weldments

Co–AgCu welds possess five distinct regions: the eutectic AgCu

Table 3
Finite element parameters.

Finite element model	Minimum seed (mm)	Maximum seed (mm)	Curvature control	Max step deflection (mm)	Max total deflection (mm)	Dominant element type	Other element type
Tension, average (long test piece)	0.1	0.125	0.2	0.005	1.25	Hex[a]	N/A
Tension, average(short test piece)	0.1	0.125	0.2	0.005	1	Hex	N/A
Root and face bending, weakest	0.1	0.1	0.1	0.001	7	Quad[b]	Tri[c]
Root and face bending, average	0.1	0.1	0.1	0.001	7	Quad	Tri
Root and face bending, strongest	0.1	0.1	0.1	0.001	8	Quad	Tri
Root bending (residual stress study), weakest	0.1	0.1	0.1	0.001	8	Quad	Tri
Root bending (residual stress study), average	0.1	0.1	0.1	0.001	8	Quad	Tri
Root bending (residual stress study), strongest	0.1	0.1	0.1	0.001	8	Quad	Tri
Crack compliance, weakest	0.1	0.1	0.1	N/A	N/A	Quad	Tri
Crack compliance, average	0.1	0.1	0.1	N/A	N/A	Quad	Tri
Crack compliance, strongest	0.1	0.1	0.1	N/A	N/A	Quad	Tri

[a] Hexahedral.
[b] Quadrilateral.
[c] Triangular.

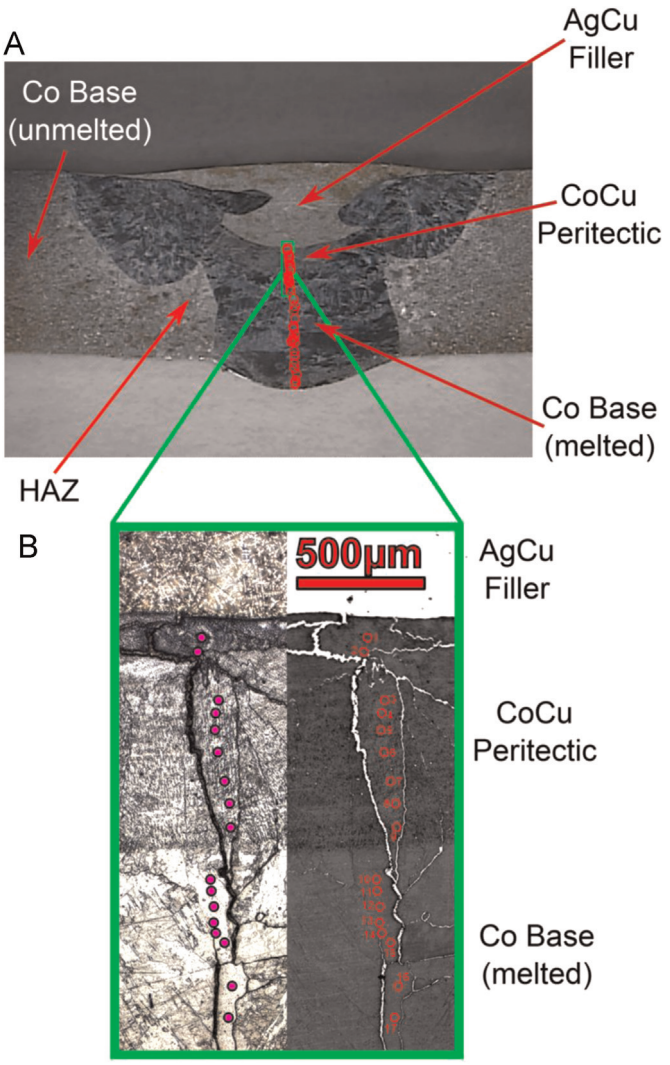

Fig. 6. (A) Weld Macrostructure (optical), (B) Microstructure (optical and backscattered SEM), and WDS Sample Locations. A: Different weld regions, as well as the location of the microprobe samples (red circles) and the magnified area to the right (green box). B: Expanded green box: AgCu filler (top), the CoCu peritectic (middle) and the Co base (bottom). The location of the WDS samples is given by purple or red dots. (For interpretation of the references to color in this figure legend, the reader is referred to the web version of this article.)

filler, the peritectic CoCu region, the melted cobalt base, the heat affected zone (HAZ), and the unmelted base (Fig. 6A). SRAS, WDS and microscopy provide a better understanding of the microstructure and origin of these zones.

The peritetic zone was originally distinguished by the presence of small (~10 μm) aligned lamellar and cellular structures, believed to be the result of Cu exsolution during cooling. These structures exist inside larger macrozones (~500 μm), which are believed to be remnant Co grains, before Cu exsolution (process by which a solid solution phase unmixes into two separate phases in the solid state).

The presence of Cu has been confirmed by WDS, with significantly higher concentrations of Cu existing in the peritectic region, which encompasses WDS measurements on spots 1–9 (Figs. 6 and 7). Optical microscopy shows two different structures inside the CoCu macrozones; close (~200 μm) to the filler these structures appear cellular, while farther away (~200–1000 μm) they are lamellar (Fig. 6). Although significant variations in Cu and Ag content occur inside the peritectic region (Fig. 7), these chemical variations are not well correlated with observed structural

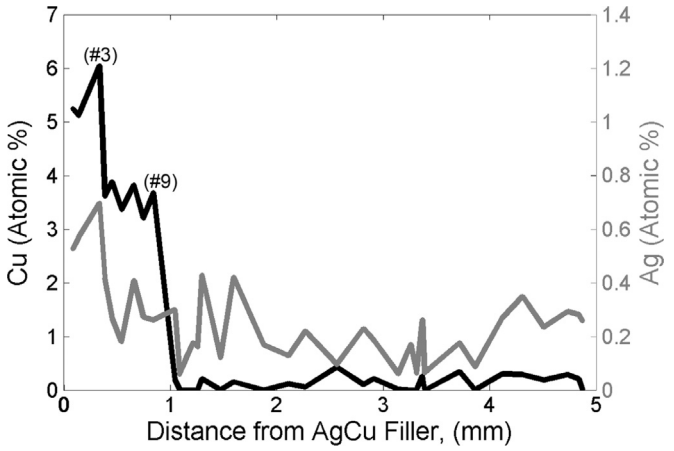

Fig. 7. Weld composition was measured using WDS, from near the base–filler interface, to the weld root. Location of the individual sample points is provided in Fig. 6. Note the high Cu concentrations (samples 1–9) existing inside the peritectic region.

differences; the area of highest Cu and Ag content extends into the lamellar region (Figs. 6 and 7). We instead believe that these structural variations are thermally induced.

SRAS also indicates that this CoCu region has a markedly different grain structure than the cobalt base. The observed macrozones in the peritectic region are generally larger than the grains in the base cobalt region, contain numerous microscopic cracks, and have a wider range of velocities (Fig. 8). Multiple regions with fast/fast (bright blue) and 'slow/slow' (pale green and salmon colors) velocity combinations exist inside the peritectic, but are absent or highly limited in the Co base.

The presence of slow/slow macrozones in the peritectic is compelling, since HCP crystal structures cannot produce this velocity combination as two orthogonal measurements cannot both be on the slow axis of the crystal. Furthermore, the presence of numerous 'fast/fast' grains indicates that the observed velocity profiles cannot result exclusively from an overall wave speed reduction.

Texturing in the peritectic region (Fig. 6), which was attributed to Cu exsolution during cooling, may help explain differences in observed wave velocity. These Cu exsolution structures are too small for SRAS detection, but maintain original grain orientation, resulting in large apparent grain size. Effects of the Cu lamella are probably a function of their orientation, complicating analysis. Furthermore, optical images taken during SRAS show this region contains numerous microscopic cracks (Fig. 8), which may also have an effect on the measured velocities. Persistent FCC Co macrozones could explain the simultaneous presence of slow/slow and fast/fast regions, although neither FCC Co, nor FCC CoCu are stable at room temperature [35]. Finally, differences in wave velocities between the peritectic and base regions may partially result from slower wave speeds in the base. The cobalt base has been subjected to multiple heat treatments below the melting point, resulting in grain fining and jagged grain boundaries (Fig. 6), as well as probable small FCC regions and possible stacking faults.

Although observed wave velocities are probably a result of all of these effects, determining their relative importance is complicated by our lack of data for a simple, as cast Co structure. However, SRAS was able to conclusively establish the existence of the CoCu peritectic region as well as the existence of macrozones inside this region.

Further analysis of these welds involved optical microscopy on top and bottom weld faces, utilizing the methods described in Section 2.5. Directional grain growth is evident on both faces, inside the melted cobalt base (Fig. 9). The weld root shows a mixture of disordered grain growth, and grain growth away from the start of the first pass. Because a back and forth pattern was used to create the welds (Fig. 1), this preferential grain growth indicates that most grain growth at this weld root occurred during the first pass, and cannot originate from subsequent passes. This observation is confirmed for most welds, and suggests that power be increased for pass 2.

The weld face shows a series of overlapping circular structures, corresponding to the dabs of filler applied during the 3rd and 4th passes (Fig. 9). These passes are performed to the side of the original J-groove (Section 2.2), and substantially extend the melted region to either side. Examination of four separate welds typically shows between 20 and 25 dabs. The grain growth indicates torch direction, and area of greatest heat. Since the grains are ordered, and the pulses are well defined, it appears that this region was not remelted by the 5th (final) pass.

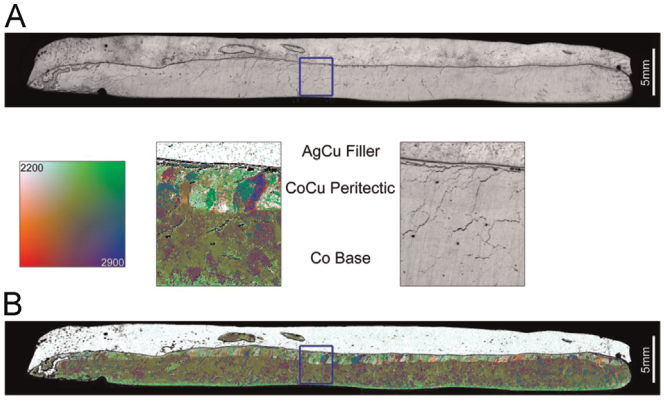

Fig. 8. Optical micrograph (A) and SRAS velocity vector map (B) of a central, longitudinal weld section. The weld start is oriented to the left. A: Micrograph illustrating the large amount of cracking in the CoCu peritectic region, as well as the large amount of porosity near the weld start. B: Image shows the SAW sound speed. The white area to the top is the AgCu filler, which provides no acoustic data. Below the filler is the CoCu peritectic region, indicated by large, predominantly bright green macrozones. Below this is the dull green and brown cobalt base. (For interpretation of the references to color in this figure legend, the reader is referred to the web version of this article.).

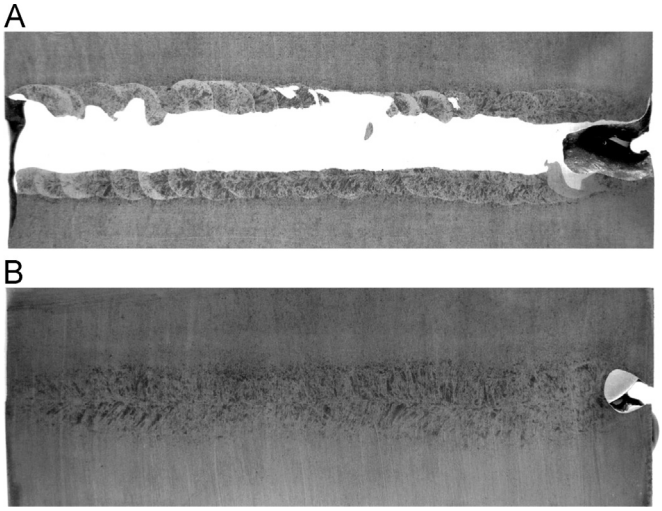

Fig. 9. Weld macrostructure revealed by polishing slurry. Weld start is at left. A: Weld face showing filler pool (white) surrounded by cobalt. Each semicircle corresponds to a dab of filler applied to the weld. The overlapping semicircles indicate pass direction. B: Weld root showing directional grain growth corresponding to the initial pass.

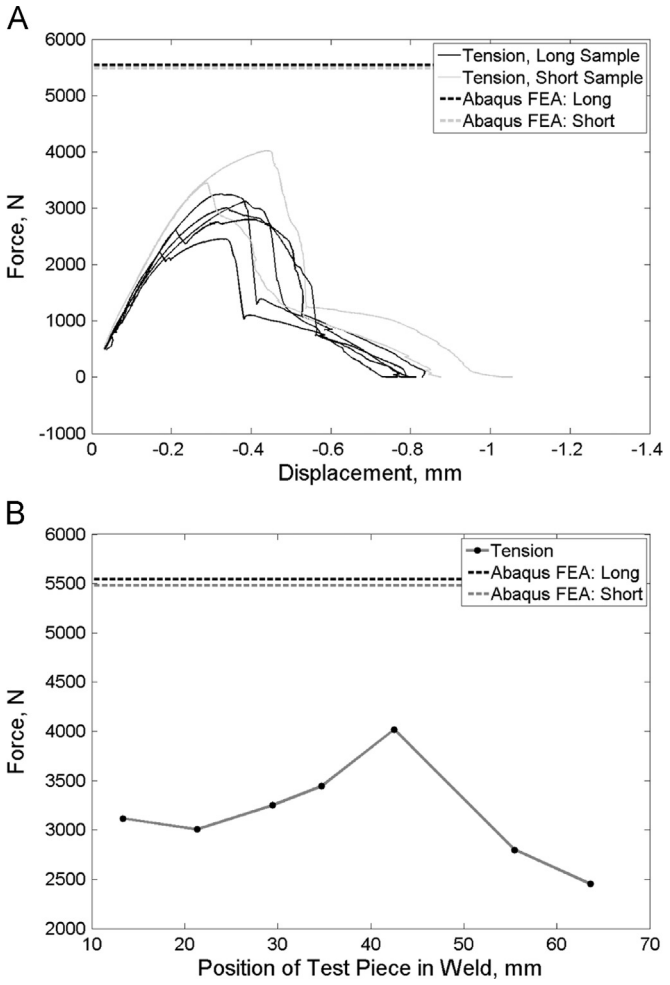

Fig. 10. Tension tests and finite element analysis. A: Horizontal dotted lines show predicted failure for the long test piece (dark) and the shorter test piece (gray). Solid lines show the measured force/displacement curve during tensile failure. B: Plot showing ultimate tensile force vs. test piece position, and FEA predicted failure. Test pieces in the center of the weldment are significantly stronger, unlike most other tests which show a quasi-steady region.

3.2. SEM, FEA and fracture of tensile specimens

A single weld was sectioned into two long and five short test pieces for tensile testing (Fig. 2). Although the different test piece geometries will effect displacements and observed stiffnesses, there should be little effect on ultimate failure strength. FEA of these two geometries confirms this assertion; predicted failure strength of the shorter and longer test pieces were 5485 N and 5544 N respectively. This 1% difference is likely due to slight differences in observed thickness (Table 1).

The models used in this section are all three dimensional, although it would have been appropriate to use two dimensional models. This is a result of project history, rather than necessity.

Two predominant failure modes may be observed during tensile fracture (Fig. 10). We infer that the first type corresponds to the primarily brittle failure of the cobalt base, which is followed by the ductile failure of the AgCu filler (Fig. 10). The specific location of the test piece inside the weldment has a large effect on failure strength (Fig. 10). Tensile testing does not reveal the presence of a well-defined quasi-steady region. Instead, weld quality appears to increase towards the center of the weldment, in contrast with observations during 4-pt bending.

There is reasonable correlation of failure strength with FEA, in that observed failures occur between 44% and 73% of the predicted

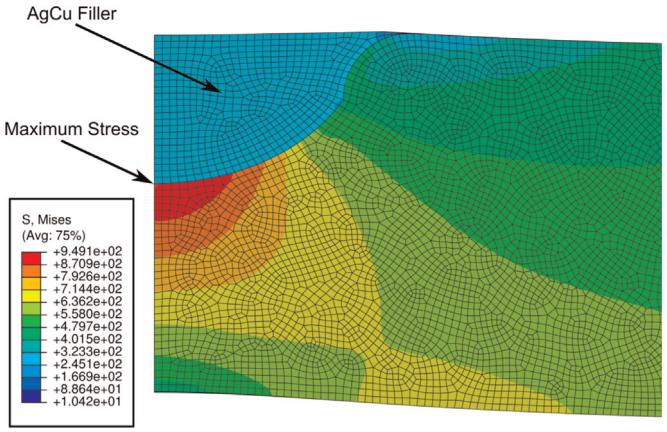

Fig. 11. Distribution and magnitude of von Mises stresses during tensile failure. Note the high stress concentration in the cobalt, immediately below the filler region. This corresponds to the CoCu peritectic region on the actual welds.

load (Fig. 10). This difference is larger than the discrepancies observed between FEA and 4-point bending. This discrepancy is likely due to both the lamellar structure of the CoCu peritectic (Fig. 6), and the large amount of cracking there (Fig. 8). This region plays only a limited role in failure during face or root bending, but is subject to high stresses in tension, and is the predicted initial location of failure (Fig. 11).

Fractography of these tensile specimens further illustrates the microstructural details of these failure types (Fig. 12). SEM of the AgCu filler shows primarily dimples (Fig. 12A) associated with void initiation, growth and coalescence, typical of ductile failure. Additionally, the filler possesses several smooth voids (Fig. 12, arrows V). These structures are believed the result of cobalt nodules observed in the filler [1], generally close to the base–filler interface. EDS shows these dimples to be composed of silver rich AgCu (Table 4), when compared with the Ag–40 at%Cu wire. This discrepancy probably results from Cu diffusion across the base–filler boundary; however, this observation is not definitive due to porosity–induced uncertainties. Cu diffusion into the Co base is supported by WDS (Fig. 6), and by the subsequent EDS measurements having a much higher Cu/Ag ratio than the filler wire.

In contrast with the AgCu filler, the CoCu peritectic possesses features associated with both brittle and ductile failure (Fig. 12B). This region is characterized by cleavage steps, covered with shallow dimples (Fig. 12B). The cleavage steps are consistent with brittle failure of lamellar structures, such as those observed in other welds (Fig. 6B). The dimples suggest the presence of a ductile layer of AgCu, an observation supported by high concentrations of AgCu measured by EDS (Table 4). These concentrations along this failure surface greatly exceed the AgCu concentrations measured by WDS of the weld section (Fig. 7), which also suggests that failure has occurred along a small AgCu layer, such as a backfilled crack.

The combination of brittle and ductile failure modes is also observed further from the filler (Fig. 12C). This region is suspected to consist of relatively pure cobalt (Fig. 7), with intermixed AgCu cracks, although the fractograph does not permit definitively determining the border of the Co base and CoCu peritectic. Brittle failure is evidenced by multiple facets, whereas dimples, like before, indicate a ductile failure mechanism. EDS measurements show varying concentrations of AgCu; notably an area with no dimples (Table 4, #6) has a much lower AgCu concentration. We again ascribe the observed failure, as well as the high AgCu concentrations, to the failure of a backfilled crack.

Failure mechanisms even further from the filler appear brittle (Fig. 12), corresponding to the general lack of backfilled cracks in

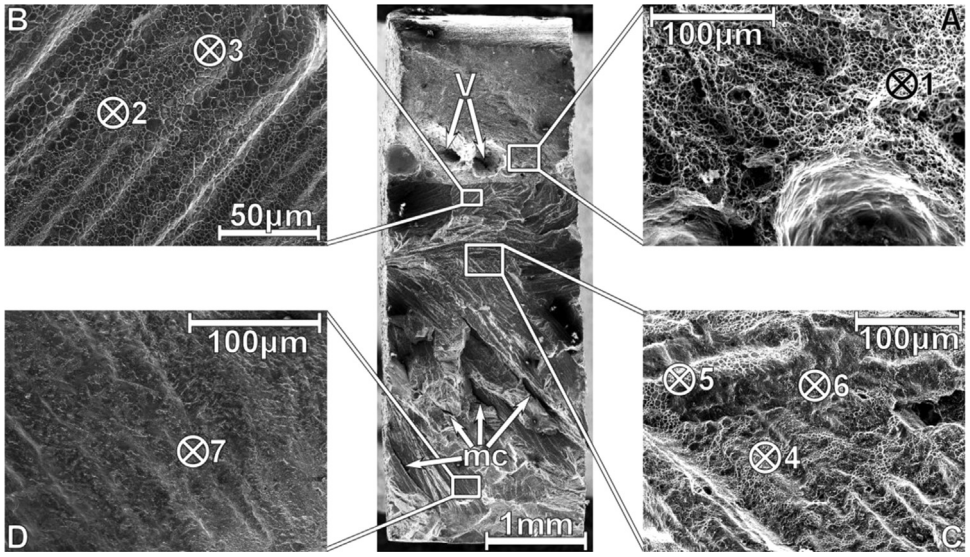

Fig. 12. SEM fractography of tensile failure surface. Voids (V); Microcracks: (mc). A: Ductile failure of the AgCu filler (dimples ~5 μm). Large smooth voids are probably the result of Co nodules near the base–filler interface. B: Failure of a suspected backfilled AgCu crack surrounded by the CoCu peritectic. Cleavage is thought to result from the brittle failure of the lamellar peritectic, while dimples result from the ductile failure of a AgCu backfilled crack. C: Failure of a backfilled AgCu crack, believed inside the Co base region. Facets probably result from brittle failure of the Co, while dimples result from ductile failure of the AgCu. D: Primarily brittle failure of the Co base, far from the base–filler interface. Failure appears to be intergranular.

Table 4
Material composition by region.

Location	Region	Co (at%)	Ag (at%)	Cu (at%)
1	AgCu filler	0	64	36
2	CoCu peritectic	48	28	23
3	CoCu peritectic	44	27	30
4	Co base	51	24	24
5	Co base	46	23	31
6	Co base	88	4	8
7	Co base	97	0	3

the weld root (Fig. 8). The Co base has multiple microcracks (Fig. 12, arrows mc) and facets, both associated with brittle failure. Closer examination shows a relatively flat failure surface, devoid of dimples (Fig. 12D). We tentatively ascribe this to intergranular failure. EDS confirms this fracture surface is composed of nearly pure Co, although a small amount of Cu is observed, which may have segregated along a grain boundary.

3.3. Fracture of unground weld in root bending

A single weld was cut into 20 sections for 4-point root bending tests (Fig. 4). These results were compared to the completed weld from [1], in order to verify the quality of our newer welds, as well as the approximate location of the quasi–steady zone. Because the sections used have different widths, the reported loads have been normalized by width. The quality of the newer weld appears superior, which failed at higher displacements and normalized loads than previously (Fig. 13). If the region between 31 and 54 mm is considered, the newer weld fails, on average, at a 16% higher load. This improvement is not surprising, due to the large amount of practice the welder had between the 5 pass weld produced for our previous study, and this one.

More importantly, this test indicates the location of the quasi steady zone, and the expected variability between sections. The quasi-steady zone is a region in the center of the weld which experiences homogenous thermal conditions. The presence of a quasi-steady zone generally results in stronger welds, and more consistent behavior. This region appears to begin between 29 and 31 mm, and

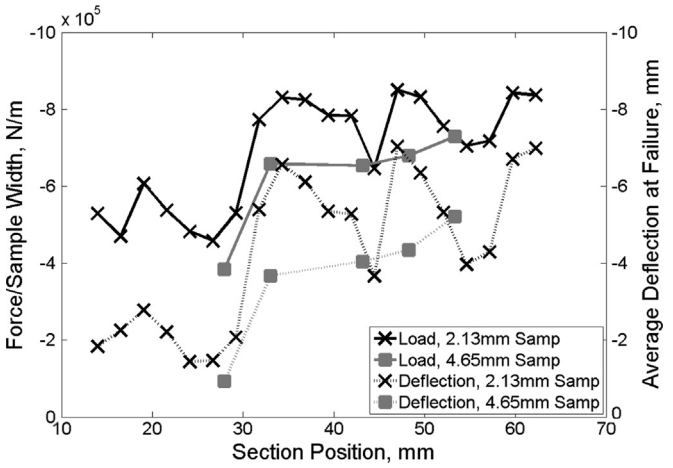

Fig. 13. Failure strength and displacement of sections from unground welds in root bending. Sections from the unground weld from this study (X), are compared to a weld from the previous paper [1] (Square).

to extend beyond the last section at 62 mm. This is a highly subjective evaluation, which may vary considerably from weld to weld.

Inside this quasi-steady region, this newer weld is notably less consistent than the original. This is mostly due to the reduction in section size, which increases the importance of cracking, and other random structural anomalies. Overall, the standard deviation inside the quasi-steady zone is approximately 8% of the average force at failure for a 2.13 mm thick section.

3.4. Fracture, SEM and FEA of welds in face and root bending

Three welds were ground and cut into 21 sections for 4-point face and root bending tests (Fig. 4). The best and worst examples for each of these tests was imaged using the SEM. Finite element models were also made for both of these tests.

Grinding of these welds was performed in order to make their geometry uniform, and to simplify comparison with our residual stress tests. However, removal of the weld root will weaken these welds and potentially change the site of initial failure.

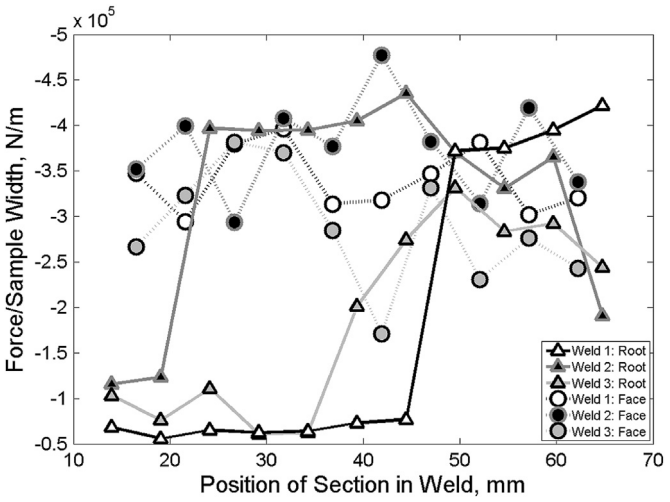

Fig. 14. Failure strength for sections in three ground welds in alternating face and root bending. Face bending (dotted line) is much more consistent then root bending (solid line), and does not have an obvious dependency on section position.

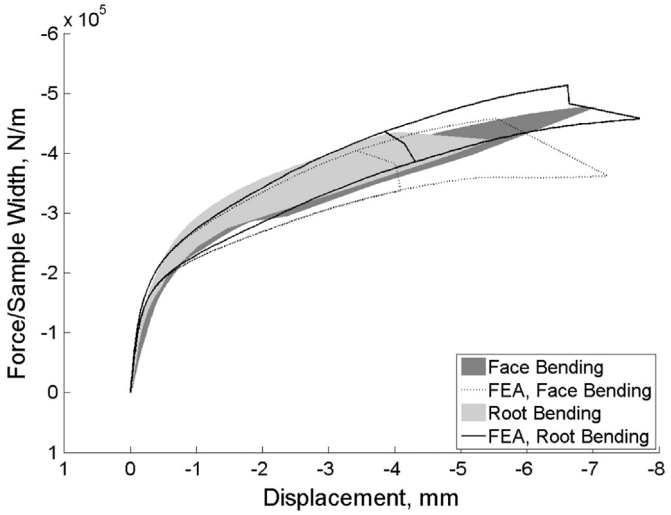

Fig. 16. FEA predicted failure curves (outline) and observed curves (solid) for face and root bending. The boundaries of the FEA curves were determined using our 3 separate models. The middle division shows the onset of failure in the filler, due to excessive plastic deformation. The solid regions were calculated using only sections exhibiting cobalt failure.

Face bending results in fairly consistent behavior across the weld, with no significant positional dependence (Fig. 14). Root bending exhibits a much higher degree of variability (Fig. 14), with a strong dependence on section position. The sections located close to the weld start have a much lower strength than later sections for all three welds. This difference can be interpreted as a result of the varying thermal fields at the beginning of the welding process. The size of this weakened region varies, from approximately 20–45 mm, depending on the particular weld. The strongest weld has another decrease in strength towards its end, which is likely the result of higher temperatures at the end. The lack of this marked decrease for the other welds implies that their lower strength is caused by inadequate heating.

Finite element analysis reveals two possible mechanisms for failure in root bending. Excessive stress at the center of the weld root (Fig. 15A) can cause failure of the cobalt base in tension, or contribute to the failure of preexisting cracks. Previous FEA predicts weld failure to occur on one side of the weld root [1], this difference is believed due to the effects of grinding the weld prior to fracture. FEA also predicts failure via excessive, compressive deformation of the filler (Fig. 15B), however this mechanism does not appear to be as significant.

Predicted failure in face bending also occurs via two separate mechanisms. Excessive deformation of the filler adjacent to the base/filler boundary (Fig. 15D) may contribute to weld delamination, or tensile failure of the filler. Failure of the cobalt base in compression is also predicted (Fig. 15C).

Three separate models were created in order to estimate the uncertainties in the force vs. displacement curves (Tables 1 and 3). These models show slightly higher forces and displacements at failure in root bending than face bending (Fig. 16). Trends closely follow predicted behavior for both face and root bending, if the poorest quality root bending samples are excluded. However, observed displacements in root bending are generally lower than face bending (Fig. 14), implying that failure is occurring prematurely due to material quality.

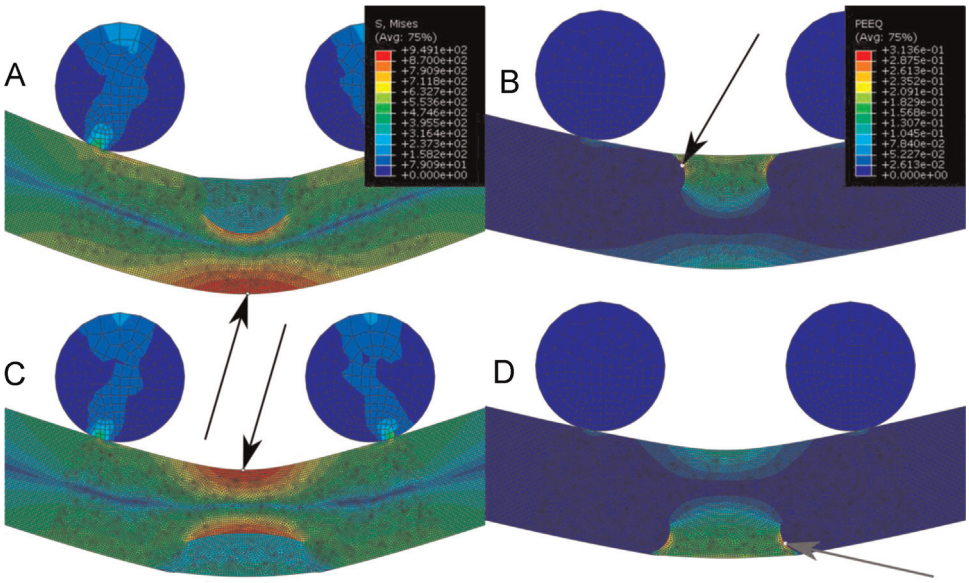

Fig. 15. FEA of Root and Face Bending showing only 2 of the 4 rollers (compare with Fig. 3) All models utilize the average geometry (Table 2). Maximum values indicated by arrow. A: FEA showing predicted von Mises stress at failure in root bending. B: FEA showing equivalent plastic strain (PEEQ) at failure in root bending. C: FEA showing predicted von Mises stress at failure in face bending. D: FEA showing equivalent plastic strain (PEEQ) at failure in face bending.

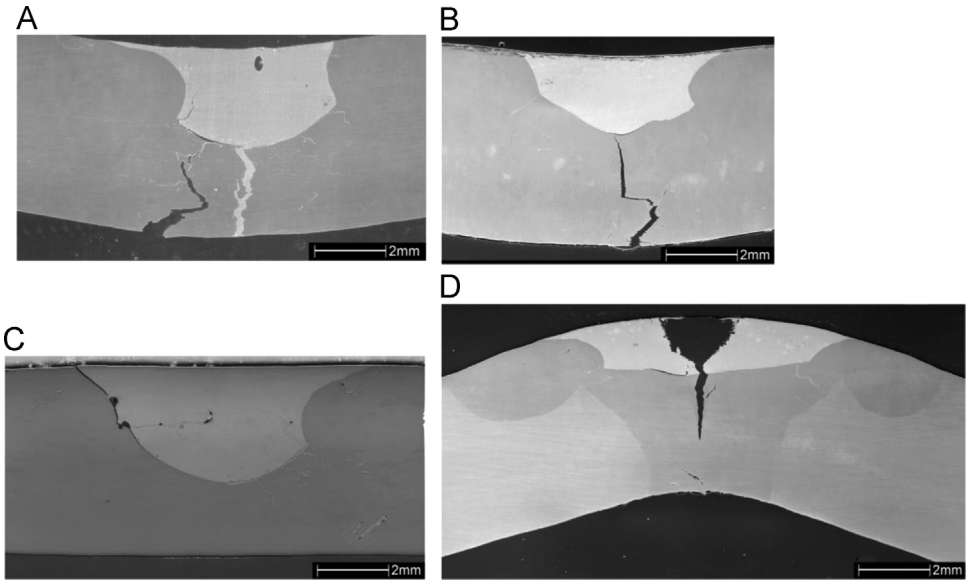

Fig. 17. SEM of failures in root and face bending. A: The weakest section in root bending. Note the number of backfilled cracks in the cobalt base. Examination of the failure surface reveals porosity, and the presence of preexisting cracks without AgCu backfill. B: The strongest section in root bending. Note the matching failure surfaces of the crack. The straight failure, under the filler region, implies intergranular fracture. C: The weakest section in face bending. Note the number of voids and imperfections, especially along the base/filler boundary. Failure appears predominantly by delamination. D: The strongest section in face bending. An outline showing the melted cobalt is also observed. Failure is predominantly central, and excessive necking of the AgCu filler is observed. Some delamination occurs, but this does not appear to be predominant. Note also the shear failure of the cobalt root.

SEM images of the strongest and weakest weld sections illustrate the effects of defects and geometry (Fig. 17). The weakest root bending section failed via cracking in the cobalt base (Fig. 17A), consistent with FEA predictions. However, failure occurred at substantially lower load than predicted, suggesting that material quality of this specimen is low. Base–filler delamination also occurred, most likely after initial failure. This section also has large backfilled cracks, evidence of voids along the failure surface, and smaller, open cracks. It also has a large filler region, which will contribute to a high stress concentration in the base. The failure surface follows a small preexisting, backfilled crack close to the filler. Although it is not possible to conclusively establish the presence of cracking before flexure, the presence of other, open cracks suggests that failure followed a preexisting open crack.

In contrast, the strongest section (Fig. 17B) has a smaller than average filler region, and only minimal backfilled cracks, toward the side of the weld. As before, delamination has occurred after failure. Failure below the filler appears is centered and straight, suggesting that it has occurred along the centralized grain boundaries.

The weakest face bending section (Fig. 17D) also exhibits significant defects, as well as a larger than average filler region. In this case, failure occurred via base–filler delamination. The boundary has several significant voids which are directly along the path of failure. The filler pool also has several voids, which appear to play a minor role in failure, due to the presence of a horizontal crack. The presence of voids along the base–filler boundary suggests poor base–filler adhesion. Furthermore, the shape of the left side is not consistent with the general shape observed in these welds, indicating an error in welding technique.

The strongest face bending section (Fig. 17D) was imaged after 0.03 μm polishing, revealing this weld's basic macrostructure. Overall, the geometry of this weld resembles the weld produced in the previous study (Fig. 6A). The darker gray region indicates the extent of melting, which is roughly symmetric. The filler pool is small, increasing the amount of cobalt available. Backfilled cracking is observed, but occurs only to the side of the filler pool. Some delamination is also observed, as well as intergranular, tensile failure and shear failure in the base. However, the main mode of failure involves necking of the filler. The high strength of this weld section is due to a combination of favorable geometry, adequate adhesion, and high quality materials.

In all cases, weld quality is clearly influenced by geometric factors and material imperfections. The large amount of discrepancy in the root bending test is due to the cobalt base being prone to cracking. This behavior results in much greater sensitivity of the root bend test to thermal differences during weld manufacture. The face bending test is also subject to similar effects, but the ductile filler is unlikely to form cracks. The defects most likely to cause poor performance are voids in the filler, and along the base filler boundary.

3.5. *Residual stress, heat treatment, and root bending*

Four welds were ground and cut into 7 sections for heat treatment, residual stress measurement, and root bending tests (Fig. 4). Grinding our residual stress sections into a consistent cross section is essential for analysis, but will potentially alter residual stresses. Two separate regions were defined for each weld; each region was either left as is, or subjected to a 325 °C heat treatment for 100 h. Five of these welds had their residual stresses measured by crack compliance; data reduction was performed using FEA.

This low level heat treatment had no statistical effect on strength. If all samples are considered, the *t*-test reveals a 24% likelihood strengths are influenced by heat treatment. If we remove the Sections 1 and 2 from every weld, in order to reduce the effect of material defects, the probability of this being a random distribution rises to 92%.

Residual stress measurements were successfully completed on 5 sections (Fig. 18). Two of these sections have a slitting error at approximately 0.1 mm. While this error is far from the area of interest, it does affect the trends at the beginning of the plot. For these samples we only report maximum stresses (Table 5).

Heat treatments do not appear to have affected the maximum stresses (Table 5). This conclusion correlates with earlier observations in four-point bending. The welds are subjected to

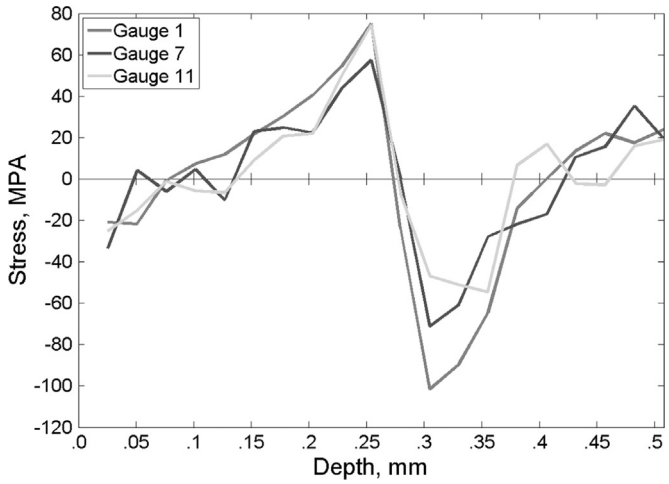

Fig. 18. Measured residual stresses vs. EDM cut depth. The top of the section is at a depth of zero; the AgCu filler is located at low depth, and the Co base begins at around 0.3 mm. Note the large tensile stresses in the filler, opposite the large compressive stresses in the base, which change into a small area of tensile stress in the weld root.

multiple welding passes at significantly higher temperatures than our heat treatment, thereby limiting its effectiveness.

The residual stress profile observed is unlikely to influence failure. The areas of high stress are in the sample center, along the base–filler interface (Fig. 18). According to both our FEA predictions (Fig. 15), and SEM observations (Fig. 17), this region is not the location of failure in bending. Furthermore, these stresses place the CoCu peritectic under compression, which should strengthen the region during tensile tests. In general, compression in this area is expected to be beneficial, considering the large amount of pre-existing cracks (Fig. 8), and the tendency of cobalt to experience brittle failure. Limited tensile residual stresses exist at the weld root (Fig. 18, Table 5); according to our finite element analysis, these stresses are the correct direction to influence failure during root bending. However, these stresses average only 28.7 MPa, which is approximately 3% of the failure strength; much less than effects of geometry and imperfections. Due to the nature of the crack compliance method, it is not possible to measure residual stresses occurring at the very end of the sample, nor is it possible to measure stresses in the area removed by grinding. However, residual stress trends toward the weld root are relatively flat, indicating that the above estimate is reasonable. As such, effects of these stresses upon failure have not been observed.

4. Conclusions

The failure of Co–AgCu weldments was investigated by comparing SRAS, WDS, and microscopy to finite element models and to residual stress data, for welds fractured in tension and four-point bending in both the root and face bending orientations. SEM suggests that failure is mainly a result of weld imperfections and geometric differences. Chief among these are cracking and porosity. These imperfections are much more prevalent in the base pool than the filler pool, resulting in more consistent behavior for the specimens subjected to face bending than to root bending. Finite element modeling predicts loads at failure which are only marginally higher than actual failure loads for best tested specimens. This is consistent with random imperfections heavily influencing failure. Failures in tension exhibit the highest difference between predicted and observed behavior. This is probably the result of the lamellar structure and high prevalence of cracks in the CoCu peritectic region, which were observed using SEM, optical microscopy, and SRAS. This region experiences only small stresses during bending, which reduces the effects of imperfections.

Although the effect of local geometry is probably more important than residual stresses under fatigue loading, this assertion has not been verified by this study, and is not certain. The welds examined here have complex microstructures with multiple failure mechanisms. Relating the geometry, microstructure and failure mechanism was not trivial; producing additional data on fatigue loading is highly desirable, since most welds operate under varying loads. Some data in literature already exists. Berto and Lazzarin [23] show how fatigue life is affected by the strain energy density. As it increases, the fatigue life is correspondingly decreased (in particular, Figs. 8–10 of [23]).

Statistically, heat treatment neither affects strength, nor maximum residual stress. The heat treatment was kept at a low temperature (325 °C) to prevent cobalt from entering the high temperature FCC phase. Because the temperature was low, no geometric changes or grain refining could occur during heat treatment. However, during welding, they experience five separate passes at much higher temperatures. The final, 5th pass functions as a high-temperature heat treatment for the cobalt base, which is unlikely to experience significant melting. We infer that this final pass prevents the subsequent, low temperature heat treatment from having observable effects on either the residual stresses or failure strengths.

Residual stresses were also shown not to affect weld strength in four-point bending. This is likely due to random imperfections being an over an order of magnitude more important than the residual stresses. Furthermore, the maximum stresses occur in the center of the weld, immediately under the base–filler interface, which is an area not significant to failure in bending. The stresses in the cobalt base are predominantly compressive; changing them is therefore unlikely to affect failure in tension or bending. The corresponding tensile stresses in the filler are also unlikely to observably affect failure due to the high ductility of the AgCu filler.

The surrogate approach presented earlier [1] and here is a viable method to investigate weldments of toxic metals using safe substitute materials. The criteria for choosing the surrogates include: same crystallographic structure, similar differences in CTA, melting points of base and filler, miscibility of base/filler. The concept of surrogate welding may be applied to exotic welds.

Table 5
Residual Stress, MPa.

Gauge	Weld	Section	Type	Heat treated	Maximum tensile	Maximum compressive	Maximum tensile, root
1	1	7	Temperature	Yes	75.14	−101.7	23.91
7	3	7	Temperature	No	57.58	−71.3	35.28
8	2	4	Time	Yes	71.1	−78.75	29.74
9	3	2	Time	No	51.61	−80.74	41.45
11	1	4	Temperature	No	74.5	−54.6	18.87

Acknowledgments

We would like to thank Craig Hobson for his welding skill and expertise, Bin Wang for her SEM images, and Anne Hofmeister and Robert Criss for valuable discussion. We would also like to thank Los Alamos National Laboratory for their support.

References

[1] E.M. Criss, M.A. Meyers, Braze welding of cobalt with a silver–copper filler, J. Mater. Res. Technol. 4 (1) (2015) 44–59.
[2] M.E. Kolanz, Introduction to beryllium: uses, regulatory history and disease, Appl. Occup. Environ. Hyg. 16 (5) (2001) 559–567.
[3] W.F. Gale, T.C. Totemeier (Eds.), Smithells Metals Reference Book, 8th ed., Butterworth-Heinemann, Oxford, 2003.
[4] ASM specialty handbook, nickel, cobalt and their alloys, ASM, Materials Park, 2000.
[5] Cobalt Monograph, Center D'Information du Cobalt, Brussels, 1960.
[6] Cobalt Facts, Cobalt Development Institute, 2013.
[7] K.B. Shedd, Minerals Yearbook, Cobalt (advance release) 2011, United States Geological Survey, 2013.
[8] P. Campbell, Permanent Magnet Materials and Their Application, Cambridge University Press, Cambridge, 1996.
[9] D.P. NaBadalung, J.I. Nicholls, Laser welding of a cobalt–chromium removable partial denture alloy, J. Prosthet. Dent. 73 (3) (1998) 285–290.
[10] M.I. MacEntee, E.B. Hawbolt, J.I. Zahel, The tensile and shear strength of a base metal weld joint used in dentistry, J. Dent. Res. 66 (2) (1981) 154–158.
[11] J. Black, G. Hastings (Eds.), Handbook of biomaterial properties, Chapman & Hall, London, 1998.
[12] E.R. Buchanan, An overview of hardfaced coatings for industrial use, in: Proceedings of the Third International Pump Symposium, College Station, Texas, May 1986 pp. 91–96.
[13] M. Riddihough, Stellite as a wear-resistant material, Tribology 3 (4) (1970) 211–215.
[14] A. Roth, Vacuum Sealing Techniques, AIP Press, Woodbury, 1994.
[15] O. Untracht, Jewelry Concepts & Technology, Doubleday, New York, 1985.
[16] J.R. Davis (Ed.), Alloying: Understanding the Basics, ASM, Material Park, 2001.
[17] M.J. Donachie, S.J. Donachie, Superalloys: a Technical Guide, 2nd ed., ASM, Materials Park, 2002.
[18] S.C. Levy, P. Bro, Battery Hazards and Accident Prevention, Plenum Press, New York, 1994.
[19] M.A. Laughton, D.F. Warne, Electrical Engineer's Reference Book, 16th ed., Elsevier, Oxford, 2003.
[20] J. Sato, T. Omori, K. Oikawa, I. Ohnuma, R. Kainuma, K. Ishida, Cobalt-base high-temperature alloys, Science 312 (7) (2006) 90–91.
[21] H.-Y. Yan, V.A. Vorontsov, D. Dye, Alloying effects in polycrystalline γ' strengthened Co–Al–W base alloys, Intermetallics 48 (2014) 44–53.
[22] P. Lazzarin, F. Berto, Some expressions for the strain energy in a finite volume surrounding the root of blunt V-notches, Int. J. Fract. 135 (1–4) (2005) 161–185.
[23] F. Berto, P. Lazzarin, A review of the volume-based strain energy density approach applied to V-notches and welded structures, Theor. Appl. Fract. Mech. 52 (3) (2009) 183–194.
[24] F. Berto, P. Lazzarin, Recent developments in brittle and quasi-brittle failure assessment of engineering materials by means of local approaches, Mater. Sci. Eng.: R: Rep. 75 (2014) 1–48.
[25] R.J. Smith, W. Li, J. Coulson, M. Clark, M.G. Somekh, S.D. Sharples, Spatially resolved acoustic spectroscopy for rapid imaging of material microstructure and grain orientation, Meas. Sci. Technol. 25 (5) (2014) 055902 11 pp..
[26] W. Li, S.D. Sharples, R.J. Smith, M. Clark, M.G. Somekh, Determination of crystallographic orientation of large grain metals with surface acoustic waves, J. Acoust. Soc. Am. 132 (2) (2012) 738–745.
[27] J.T. Plewes, K.J. Bachmann, The effect of thermomechanical pretreatment on the allotropic transformation in cobalt, Metall. Trans. 4 (1973) 1729–1734.
[28] Casti Metals Blue Book, Welding Filler Metals, 4th ed., Casti Publishing, Alberta, 2003.
[29] Standard Test Method for Guided Bend Test for Ductility of Welds, Designation: E190-92, ASTM International, 2008.
[30] J.T. Armstrong, Citzaf-a package of correction programs for the quantitative electron microbeam X-ray analysis of thick polished materials, thin films, and particles, Microbeam Anal. 4 (3) (1995) 177–200.
[31] Q. Meng, S. Guo, X. Zhao, S. Veintemillas-Verdaguer, Bulk metastable cobalt in fcc crystal structure, J. Alloy. Compd. 580 (2013) 187–190.
[32] Y.Z. Tian, S.D. Wu, Z.F. Zhang, R.B. Figueiredo, N. Gao, T.G. Langdon, Microstructural evolution and mechanical properties of a two-phase Cu–Ag alloy processed by high-pressure torsion to ultrahigh strains, Acta Mater. 59 (2011) 2783–2796.
[33] M.R. Hill, The slitting method, in: G.S. Schajer (Ed.), John Wiley & Sons Ltd, Chichester, 2013.
[34] M.B. Prime, Experimental Procedure for Crack Compliance (Slitting) Measurements of Residual Stress, LA-UR-03-8629, Los Alamos National Laboratory, 2003.
[35] T. Nishizawa, K. Ishida, Co-Cu (cobalt–copper), in: 2nd ed.,in: T.B. Massalski (Ed.), Binary Alloy Phase Diagrams, vol. 2, ASM International, Materials Park, 1990, pp. 1181–1183.